Solar RRL

RESEARCH ARTICLE OPEN ACCESS

An Interconnection Strategy for Thermally Sensitive Solar Cells Employing Electrically Conductive Tape

Yanxin Liu[1,2] | Andreas Lambertz[1] | Ian Marius Peters[1] | Unisa Adikalie Kargbo[1] | Bart Pieters[1] | Benedikt Fischer[1,2] | Henrike Gattermann[1] | Xuanlei Du[2] | Volker Lauterbach[1] | Karsten Bittkau[1] | Uwe Rau[1,2] | Kaining Ding[1,2]

[1]IMD-3: Photovoltaics, Forschungszentrum Jülich GmbH, Jülich, Germany | [2]Jülich Aachen Research Alliance (JARA-Energy) and Faculty of Electrical Engineering and Information Technology, RWTH Aachen University, Aachen, Germany

Correspondence: Yanxin Liu (ya.liu@fz-juelich.de) | Kaining Ding (k.ding@fz-juelich.de)

Received: 4 November 2025 | **Revised:** 12 June 2026 | **Accepted:** 13 August 2026

Keywords: contact resistance | electrically conductive tapes | low-temperature interconnection | perovskite-SHJ tandem solar cell | silicon heterojunction

ABSTRACT

The electrical interconnection of high-efficiency silicon heterojunction and perovskite–silicon tandem solar cells is constrained by their sensitivity to elevated processing temperatures, which precludes the use of conventional solder-based interconnections. As a low-temperature alternative, electrically conductive tapes (ECTs) offer a promising solution; however, their applicability in photovoltaic modules has been underexplored. This study evaluates the feasibility of commercially available ECTs as solder-free interconnection materials for silicon heterojunction solar cells. To assess their performance, we characterized the effects of lamination pressure and temperature on adhesion and electrical contact resistance, followed by rigorous long-term stability testing under damp heat (2000 h) and thermal cycling (200 cycles) per IEC 61215 standards. Anisotropic ECTs demonstrated low and stable contact resistances, comparable to those of low-melting-point solders, while also exhibiting robust mechanical durability. Among the tested materials, ECT-2 exhibited the highest adhesion strength, achieving a peak value of 1.8 N/mm, whereas ECT-3 provided the lowest and most consistent contact resistance. Specifically, ECT-3 maintained contact resistance values in the range of 10^{-3}–10^{-2} mΩ·cm^2 throughout both damp heat and thermal cycling tests, matching the performance of soldered interconnections. Silicon heterojunction modules utilizing ECT-based interconnections showed superior stability during accelerated aging, with efficiency losses below 5%, outperforming both isotropic tapes and soldered references. Furthermore, ECTs enabled effective electrical connections in perovskite–silicon heterojunction tandem solar cells, facilitating solder-free interconnection without the need for thermal curing. An encapsulated perovskite–silicon tandem cell with an effective area of 1×1 cm^2 achieved an efficiency of 28.6%, with unchanged open-circuit voltage (V_{oc}) and fill factor (FF). These findings underscore the potential of ECTs as a scalable, low-temperature interconnection solution for next-generation photovoltaic technologies.

1 | Introduction

The global demand for sustainable and green energy has accelerated the development of high-efficiency photovoltaic (PV) technologies. Silicon heterojunction (SHJ) solar cells and perovskite–silicon tandem solar cells are among the most promising advancements, offering the potential to surpass the efficiency limits of conventional PV modules. However, their sensitivity to elevated processing temperatures presents significant challenges. SHJ solar cells rely on hydrogenated amorphous silicon layers that degrade above 200 °C [1], while perovskite materials are prone to thermal decomposition at temperatures exceeding approximately 125 °C [2]. These thermal constraints complicate the cell-to-module interconnection process, which traditionally relies on high-temperature soldering methods. To address these limitations, low-melting-point solders, such as indium-tin (InSn) and bismuth-tin (SnBi) alloys, have been explored for SHJ interconnections [3, 4]. However, their processing temperatures often exceed the thermal tolerance of perovskite materials, and the limited availability and high cost of indium and bismuth raise concerns about scalability for large-scale PV deployment [5]. Additionally, while Sn60Pb40 solder remains in use within parts of the PV industry [6], the European Union's Restriction of Hazardous Substances (RoHS) directive mandates the phase-out of lead in electronic products to enhance environmental sustainability [7]. This regulatory shift underscores the need for alternative interconnection solutions.

Electrically conductive adhesives (ECAs) have emerged as a low-temperature (<150 °C) alternative for interconnecting perovskite-based cells. However, ECAs typically contain a large amount of costly silver. To address this, Zemen et al. proposed using an electrically conductive thermoplastic adhesive coated on Cu wires, known as the thermoplastically electrically conductive coated (TECC) wire solution [8]. Nevertheless, similar to conventional ECA solutions, this approach still requires heat curing to solidify or achieve adhesion on the surface of solar cells, posing a potential thermal risk to temperature-sensitive materials. In contrast, electrically conductive tapes (ECTs)—comprising conductive particles or mesh embedded in an adhesive matrix—enable a heat-free interconnection process [9]. Originally developed for electromagnetic interference shielding and fine-pitch interconnections in electronics, ECTs remain underexplored for PV module applications.

ECTs are available in isotropic (3D-conductive) and anisotropic (Z-axis dominant) configurations. For PV modules, particularly conventional H-pattern solar cells with front-side busbars and tabbing ribbons, anisotropic ECTs are generally sufficient. These tapes require significantly fewer conductive particles than ECAs, as only a single particle layer can electrically bridge opposing substrates, offering a cost-effective and thermally benign interconnection approach. Nevertheless, key questions remain regarding their suitability for PV applications, including whether ECTs can deliver:

- Sufficiently low contact resistance (R_c) to minimize power losses,
- Strong adhesion to meet mechanical durability standards (e.g., ≥1 N/mm as per DIN EN 50461 [10]) and
- Long-term stability under environmental stress without degradation or corrosion.

This study investigates the feasibility of commercially available ECTs as a solder-free interconnection method for thermally sensitive solar cells, with a focus on SHJ architectures. We evaluate the influence of lamination conditions (temperature and pressure) on electrical and mechanical performance, compare different ECT types, and assess their long-term reliability through damp heat (DH) and thermal cycling (TC) tests conducted in accordance with IEC 61215 standards [11]. Additionally, simulation tools are employed to quantify the impact of contact resistance on module power loss and to establish performance thresholds for reliable module design. These efforts aim to validate ECTs as a scalable, low-temperature interconnection solution for next-generation PV technologies.

2 | Methods and Sample Fabrication

Many commercially available ECTs are based on acrylic adhesive films, which are also referred to as pressure sensitive adhesive and whose adhesion can be influenced by temperature and pressure—conditions readily provided during the lamination process. Therefore, we first investigated whether the lamination parameters (pressure and temperature) can further impact both the adhesion and electrical properties (contact resistance) of ECTs after the interconnection process.

In the standard lamination process, the stack—comprising the solar cells, encapsulant films, front glass, and backsheet—is heated to 150 °C, while the laminator simultaneously applies a pressure of 750 mbar to facilitate outgassing and ensure uniform bonding of the encapsulant layers. To investigate the influence of the lamination pressure, we varied the pressure between 300 and 900 in 200 mbar intervals, while maintaining a constant temperature of 90 °C (the lower limit of lamination temperature). To evaluate the influence of temperature during the lamination process, the temperature was varied between 90 and 150 °C in steps of 20 °C at 300 mbar. The adhesion was evaluated using a peel-off test at 90° to the solar cell surface. A 2.5 cm wide ECT strip was laminated to the busbar area of the solar cells. A 1 mm silver-coated copper ribbon was then placed gently on the tape over the busbar area, with initial attachment achieved solely by the ribbon's weight. The solar cell was positioned on a glass substrate with a thermoplastic olefin (TPO) layer serving as a mechanical buffer in between. After lamination under varied conditions, the ribbons were peeled using a Zwick Roell universal machine with an accuracy of ±0.08 N.

For evaluating the electrical properties of the ECTs, the tape was assumed as a two-dimensional material in this study. The surface/interface and bulk resistances of the tape were considered as combined "contact resistance". This contact resistance can be measured using various methods, such as the Transmission Line Method (TLM) [12] and the four-point probe method [13]. TLM determines contact resistance by measuring the resistance between contacts spaced at varying distances, yielding an average value. In contrast, the four probes method directly measures the resistance of a single contact by evaluating the voltage drop and current flow, using a four-wire configuration. Since contact resistance between ribbons and busbars can vary significantly—particularly after aging—the four-point probe method was selected to provide a statistical overview of the evolution of individual contact resistance in this study.

The four-point probe sample structure used for electrical characterization is shown in Figure 1. Nine silver-coated copper ribbons, textured on both sides, were attached using the ECT to a screen-printed silver busbar on a 2 mm × 157.35 mm silicon wafer coated with 200 nm of SiO_x as the isolation layer. The V-shaped texture on the ribbon surface was designed by the manufacturer to enhance light harvesting through improved reflection. The defined contact area for each connection was 1 mm × 1 mm, corresponding to the ribbon–busbar overlap.

A constant current was supplied through one ribbon, passed through the busbar and a second contact, and exited via a second ribbon. Simultaneously, adjacent voltage probes recorded the

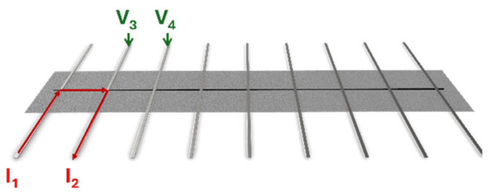

FIGURE 1 | Schematic of the sample used to measure the contact resistance between ribbons and busbars. To measure the contact resistance of the second connection, a constant current is applied between terminals 1 and 2, while the voltage drop at the contact is measured between terminals 3 and 4.

potential drop across the contact. Because some measured contact resistances were very low, currents of 0.7, 0.8, and 0.9 A were applied to increase the measurable voltage across the contact. For each current value, six measurements were performed, and the contact resistance was calculated as the average of these values. This procedure was repeated for all contacts except the first and last ones on the sample. In total, seven contact points were measured for each sample.

Since the lamination process is typically optimized for the encapsulant, it is essential to select an ECT type that is compatible with standard lamination conditions of 150 °C and 750 mbar. After initially evaluating the influence of lamination parameters on adhesion and contact resistance, three types of conductive tapes with differences in structure and conductive particle composition were compared in terms of contact resistance stability:

- **ECT-1**: A 100 μm-thick isotropic conductive tape consisting of a conductive woven fabric backing coated on both sides with conductive acrylic adhesive, also suitable for EMI shielding and grounding.
- **ECT-2**: A 50 μm-thick anisotropic conductive tape with acrylic adhesive filled with a small quantity of silver (Ag) particles. The diameter of the particles is from about 30–60 μm.
- **ECT-3**: A 10 μm-thick anisotropic tape, structurally similar to ECT-2 but filled with nickel (Ni) particles, with a diameter ranging from 20 to 50 μm. This tape was also used in the former experiment investigating the influence of lamination temperature and pressure.

The microstructure of the three types of tape can be seen under an optical microscope in Section S1.

For DH testing, two samples were prepared for each ECT type, yielding a total of 14 data points. For TC, one sample per ECT type was tested, providing 7 data points. These samples were periodically characterized during the aging tests to assess contact stability.

To benchmark ECT performance, we compared their contact resistance to joints formed using low-melting-point In52Sn48 solder, typically used in zero-busbar (0BB) solar cells. These solder-coated wires were applied to silicon strips with screen-printed silver fingers, with the contact area defined by the overlap of 250 μm-wide wires and 40 μm-wide fingers.

Given the complex degradation mechanisms in real module environments, such as corrosion, we fabricated modules with ECTs for further evaluation. For each ECT type, two modules were prepared for DH testing, and two modules for TC testing, all using half-cut industrial SHJ solar cells. The tabbing ribbons we have and used in the experiment are 1 mm wide, much wider than the ribbons in the industry, with a width lower than 0.5 mm. To balance shading and electrical loss, as well as making the module design more sensitive to contact resistance, five interconnection ribbons with antireflection (AR) features were attached to the five of the nine-busbar solar cells shown in Section S2a. To reduce costs, we investigated an ECT-saving approach: instead of applying ECT along the entire line between the ribbon and busbars, we applied ECT-2 only at the interconnection pads where the ribbons connect to the busbars. As the tape is very soft, we cut it into 3 × 1 mm strips and applied them across the busbar to better align with the positions of the buspads shown in Section S3.

For comparison, reference modules were fabricated using the same batch solar cells shown in Section S2b. In these, 18 wires were used to connect the fingers via low-melting-point InSn solder. The wires were first embedded in an interconnection foil and then laminated onto the cell to position them directly on the fingers. During the lamination process, the solder-coated wires melted and formed electrical connections with the fingers. All modules were laminated using the standard conditions previously described. The performance of the solar module was regularly monitored using an IV characterization setup, providing a measurement accuracy of ±0.36% relative in module efficiency. The aging tests were conducted in accordance with the IEC 61215 standard [11] to evaluate the degradation behavior.

To compare the adhesion performance of the ECTs, ribbons were attached to the solar cell busbars using ECTs with a length of 5 cm. Prior to testing, all samples underwent the standard lamination process, ensuring consistent processing conditions and optimal adhesion quality.

Finally, to investigate the differences in electrical and adhesion performance among the ECTs, the cross-sectional morphology of the contact region was examined using scanning electron microscopy (SEM). Samples were prepared by attaching tabbing ribbons to busbars of the solar cell using the respective ECTs, laminated without the TPO encapsulant for direct interface observation. Post-lamination, sample edges were polished via ion beam milling to create a smooth cross-section for microscopic analysis.

3 | Results and Discussion

3.1 | Simulation of the Dependence of the Contact Resistance on Module Power Output

To evaluate the impact of contact resistance on module power output, we simulated the module using PVMOS [14], configured with a metallization and interconnection layout featuring five ribbons, mirroring the experimental modules. We set a threshold of 0.1% absolute efficiency loss due to contact resistance as the

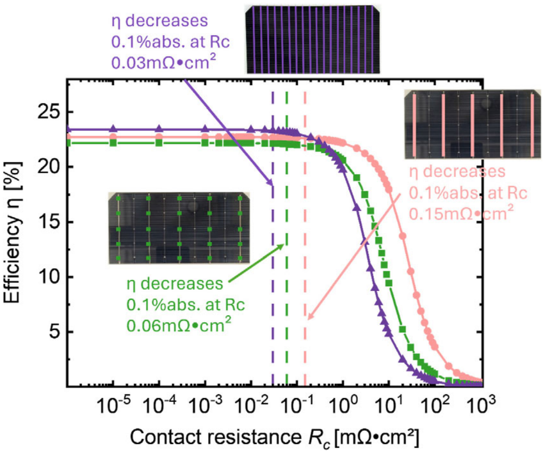

FIGURE 2 | Relationship between solar cell efficiency and contact resistance, as simulated by PVMOS. Three interconnection scenarios were simulated to correspond to the experimental module types. The pink curve represents ECT applied along the full length of the five busbars, the green curve corresponds to ECT applied only at the five buspads of the busbars, and the purple curve refers to 18 tabbing wires used with busbarless solar cells.

acceptable limit. For configurations where ECT is applied along the entire busbar (shown as the pink line in Figure 2), this limit corresponds to a contact resistance threshold of 0.15 mΩ·cm^2. However, when ECT is applied only at discrete busbar pads (shown as the green line), the contact resistance requirement becomes more stringent, requiring values no higher than 0.06 mΩ·cm^2. This difference arises because in the buspad-only configuration, current between two contact pads must traverse the thin 120 μm busbars before being extracted to the ribbons. Notably, the 18-wire configuration on busbarless M2 half-cut solar cells, despite having more contact points than the buspad-based design, demands an even lower contact resistance of approximately 0.03 mΩ·cm^2. This is due to the smaller contact area at the wire–finger interfaces, which heightens the effect of contact resistance on module performance.

3.2 | Impact of Lamination Process Parameters on Electrical Contact Resistance and Adhesion

We first investigated the general dependence of lamination temperature and pressure on the adhesion and contact resistance of the test ECT, hereafter referred to as ECT-3. Figure 3 shows the influence of the lamination pressure on the contact resistance in (a) and on the peel-off force in (b) at a constant temperature of 90 °C. Although the measured contact resistance was close to the lower detection limit of our setup, we attempted to identify potential correlations from the available data. A detailed comparison between the contact resistance of the examined ECTs and values reported in the literature will be presented in a later section. As the lamination pressure increased from 300 to 900 mbar, the median contact resistance (Figure 3a) decreased slightly from 0.003 ± 0.002 to 0.002 ± 0.002 mΩ·cm^2, with most measurements remaining below 0.005 mΩ·cm^2 regardless of pressure. Peel force values (Figure 3b) ranged from 0.13 to 0.39 N/mm, without a clear pressure-dependent trend. It should be noted that at extremely low contact resistances (<10^{-2} mΩ·cm^2), the measured R_c approached the accuracy limit of the measurement system. However, such values remain well below the defined criterion and are generally not critical for PV applications.

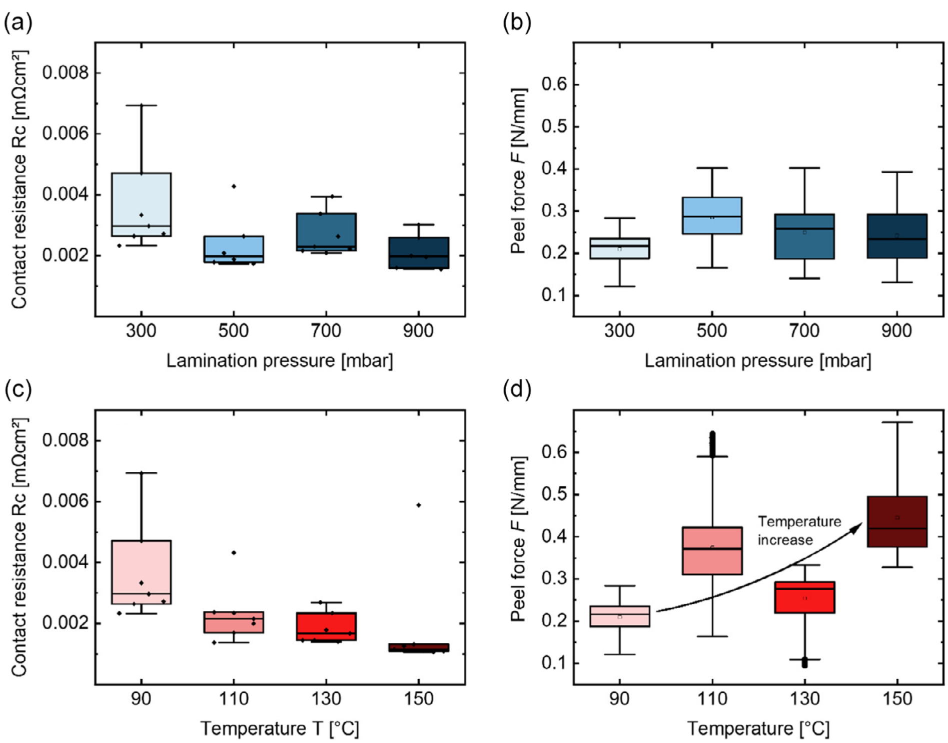

FIGURE 3 | Effect of lamination pressure on contact resistance (a) and peel force (b), and effect of lamination temperature on contact resistance (c) and peel force (d).

In contrast, Figure 3c,d show the effect of lamination temperature at a constant pressure of 300 mbar. The influence of temperature on contact resistance seems more pronounced than that of pressure. The median contact resistance decreased from 0.003 ±0.002 to 0.001 ± 0.002 mΩ·cm^2, accompanied by reduced data scatter. A similar trend was observed in the peel force measurements (see Figure 3d), with the peak peel force rising from 0.29 N/mm at 90 °C to 0.67 N/mm at 150 °C.

Overall, ECT-3 exhibited consistently low contact resistance—significantly lower than the critical values predicted by simulation in both full-busbar and buspad-only scenarios—even under minimal lamination conditions (90 °C, 300 mbar). However, its adhesion strength remained below the requirement of ≥1 N/mm, an issue that will be discussed further in comparison with other ECTs.

In general, the results suggest a correlation between adhesion and contact resistance. Higher adhesion consistently resulted in lower contact resistance values with less variation. This behavior can be attributed to the structure of ECTs, where conductive particles are embedded within the adhesive layer. Effective electrical contact is achieved when the adhesive is compressed enough to force the particles into close contact with both the solar cell and ribbon. Based on these experiments, adhesion and conductivity appear to be more sensitive to lamination temperature than pressure. Our standard lamination process (150 °C, 750 mbar) provided adequate conditions for ECT-3 to achieve its highest conductivity and adhesion. Therefore, in all subsequent experiments, the lamination parameters were kept constant.

3.3 | Stability of the Contact Resistance Under DH Conditions

Figure 4 shows the evolution of contact resistivity during DH testing for ECTs (Figure 4a) and low-melting-point solders (Figure 4b). Solid lines represent median values, while shaded regions indicate the full range of measured data. Dashed lines mark the contact resistivity thresholds corresponding to a 0.1% absolute efficiency loss. During the aging tests, some contacts did not show a gradual increase in contact resistance, but rather became completely unmeasurable, indicating failure. Figure 4c illustrates the proportion of functional contacts relative to the total number of contacts measured after aging.

The isotropic ECT-1 exhibited the highest initial contact resistance, with a median of 0.10 ± 0.005 mΩ·cm^2, and showed the fastest degradation, increasing by more than two orders of magnitude after 1000 h of DH testing. Despite this increase, all 14 contacts remained within the measurement range. In contrast, ECT-2 and ECT-3 show substantially higher stability. The median contact resistance of ECT-2 stayed close to 0.02 ± 0.002 mΩ·cm^2 even after 2000 h—twice the duration specified in IEC 61215 [11] for DH testing. ECT-3 maintained values approximately one order of magnitude lower than ECT-2, with only minor fluctuations throughout the test; however, the R_c of one of 14 contact points was out of the range of the measurement device (93% functional contacts). A general trend observed was that lower initial contact resistance correlated with reduced fluctuation during DH exposure. Both ECT-2 and ECT-3 remained below the 0.15 mΩ·cm^2 failure threshold derived from simulation, while all ECT-3 measurements were consistently below the 0.06 mΩ·cm^2 criterion for the interrupted connection scheme over the full 2000 h DH.

For comparison, low-melting-point solders exhibited contact resistances generally lower than or comparable to those of ECTs. The specific resistance of InSn solder increased slightly during aging, with the median value rising from 6×10^{-4} to 4×10^{-3} mΩ·cm^2, a similar trend to that seen with ECT-3. After 2000 h, 23 of 28 contacts (82%) show intact contact that can still be measured with our equipment. This reduced reliability is likely due to the insufficient mechanical adhesion of low-temperature solder alloys to SHJ cell metallization, particularly with Ag fine-grained structures, as reported by Rose et al. [15].

Based on the simulation, in both connection scenarios (full-line and buspad-only), modules employing ECT-3 are predicted to show negligible power loss due to contact resistance. When the median contact resistance of ECT-2 is implemented in the model, the predicted losses at the interconnects remain minimal, corresponding to approximately 0.02% absolute efficiency loss for the full-busbar configuration and 0.04% for the buspad-only configuration. In contrast, for ECT-1, assuming that module degradation arises solely from an increase in contact resistance, the simulation predicts a relative efficiency reduction exceeding 5% after approximately 500 h of damp-heat test when the tape is applied along the entire busbar.

The R_c values for isotropic ECTs in the literature range from 1 to 10 mΩ·cm^2 [16]. Variations between studies may be due to

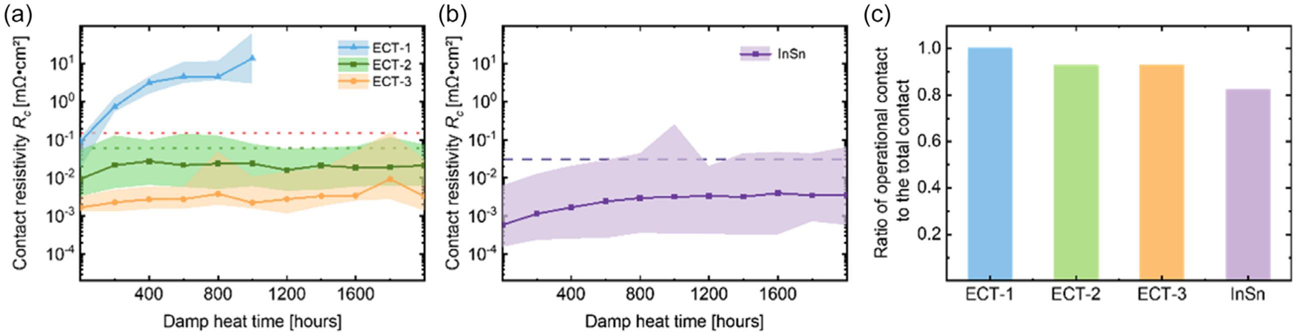

FIGURE 4 | Change of the contact resistance during damp heat testing for three types of ECT (a) and InSn solder used as references (b). The ratio of functional to total contact points is shown in (c): for ECT-1 after 1000 h, and for ECT-2, ECT-3, and InSn solder after 2000 h.

differences in measurement methodology, application process, substrate material, and substrate structure. The V-shaped texture of the Ag-coated Cu ribbon used in this study probably increased the effective contact area, which contributed to the exceptionally low R_c observed. After 200 h of DH aging, the R_c of isotropic ECT-1 in this study remains within the range reported in the literature [16].

3.4 | Stability of the Module Performance Under DH Conditions

Figure 5 shows the relative change of SHJ modules with different interconnection materials during DH testing. All modules started with an initial efficiency of approximately 23%. The module interconnected with ECT-1 (solid blue curve) exhibited the most significant efficiency decline, exceeding 5% relative after 500 h, as predicted by simulations based on measured contact resistance degradation (blue dashed line). The strong correlation between experimental module characterization and simulation results confirms that increased contact resistance was the primary cause of degradation in the ECT-1 module, leading to higher series resistance, reduced fill factor (FF), and lower power output.

After 1000 h, all other modules (ECT-2 in green, ECT-3 in orange, and multiwire with InSn-coating as reference in purple) successfully passed the DH test, exhibiting degradation of less than 3% relative. These modules show less than 5% degradation even up to 2000 h under DH conditions. The module interconnected with ECT-3, which showed the lowest and least fluctuating contact resistance in the DH test, exhibited the lowest degradation, approximately 2.5% relative, with a 1% relative reduction in FF. Modules with ECT-2, applied both along the whole busbar (green solid line) and on bus-pads (green dashed curve), showed similar degradation of approximately 4% relative efficiency and a 2% relative reduction in FF. Figure 5c shows the short-circuit current density versus DH time, all solar modules showed an almost unchanged short-circuit current density compared to initial performance. Throughout the 2000 h DH test, all modules maintained stable open-circuit voltage with a small fluctuation of less than 1% rel. in the modules with ECT-2 and ECT-3, while the V_{oc} of ECT-2D and reference modules keep almost unchanged, as shown in Figure 5d.

To investigate degradation mechanisms, electroluminescence (EL) images, captured at the I_{sc}, were compared before and after DH testing, as shown in Figure 6. The ECT-1 module showed a pronounced reduction in EL signal (dark region in the image), indicating high series resistance due to increased contact resistance. In ECT-2, ECT-2(D), and ECT-3 modules, small dark spots or circular dark areas (highlighted in green and orange rings) appeared after 2000 h, likely caused by surface contamination, as reported by Sen et al. [17]; however, this phenomenon is not the focus of the present work. In module ECT-2(D), where ECT-2 was only applied to the bus pads, slight dark areas were observed around them, highlighted in a green dashed ring. This is because the additional ECT across the bus pads partially blocks the EL signal from the cell. Picture S3 clearly shows the extra tape outside the ribbon area. Although one out of fourteen contacts in both ECT-2 and ECT-3 was nonfunctional in R_c measurements,

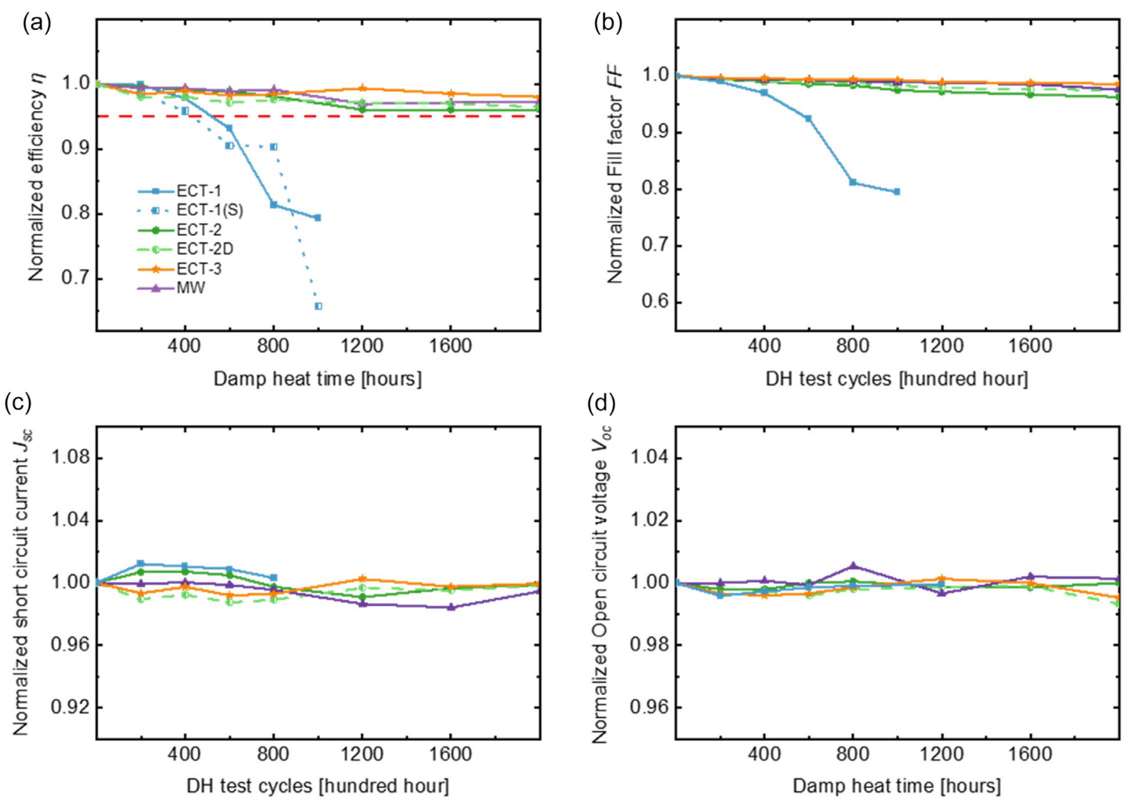

FIGURE 5 | Relative changes in (a) efficiency, (b) fill factor, (c) short-circuit current density, and (d) open-circuit voltage of SHJ modules with different interconnection methods during DH testing.

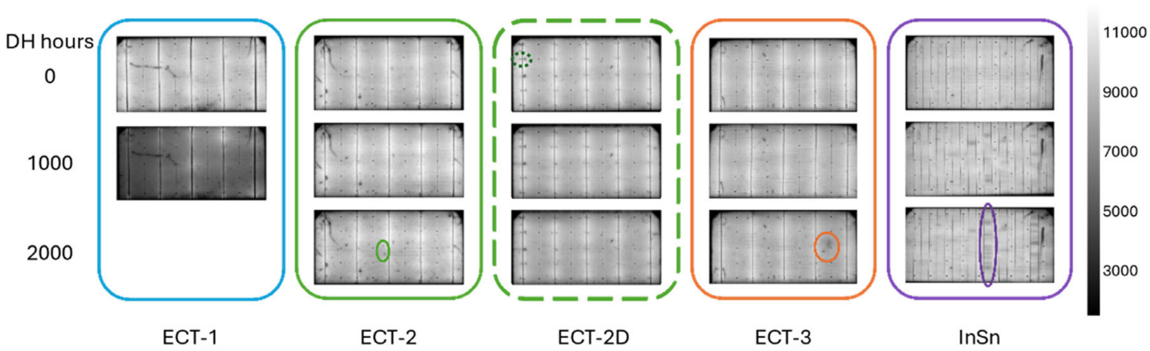

FIGURE 6 | EL images of solar modules after 0, 1000, and 2000 h of damp heat testing.

no clear darkening was observed around those contacts in EL images. In contrast, InSn-interconnected modules exhibited dark stripes between wires (marked in a purple ring), resulting from failed contacts between wires and fingers. This contact failure reduced the local current, resulting in dark areas appearing in the EL image, which also corroborated the resistance measurement results.

3.5 | Stability of the Contact Resistance and Solar Modules Performance Under Thermal Cycle Conditions

Since the ECT-1 modules failed the DH test, only ECT-2, ECT-3, and InSn modules were evaluated in the TC test, as shown in Figure 7a,b. The ratio of the contacts in takt after TC to the number of contacts in the samples is summarized in Figure 7c.

For ECT-3, the contact resistance increased only slightly over 200 cycles, with the median rising from 0.001 ± 0.002 to 0.005 ± 0.002 mΩ·cm^2. In contrast, ECT-2 showed a rapid increase in contact resistance. After 100 cycles, the minimum R_c of ECT-2 approached the 0.1% absolute efficiency loss threshold, and values were widely scattered between 0.1 and 1 mΩ·cm^2. Nevertheless, all contact points remained measurable after the TC test.

For reference, the median R_c of the modules with InSn solder increased only slightly, similar to ECT-3. However, data dispersion became large early in the TC test. After 200 industrially required cycles, one of 14 contact points exceeded the allowable limit, and 4 of 14 contacts (~29%) could no longer be measured, indicating contact breaks (Figure 7c). In comparison, all contacts for both ECT-2 and ECT-3 remained functional after testing.

The TC performance of the solar modules closely reflected changes in contact resistance. As shown in Figure 8a, the efficiency of modules with ECT-3 was comparable to that of the reference module, with absolute losses of 0.15% and 0.2%, respectively, both corresponding to less than 1% relative loss. All modules maintained stable V_{oc} and J_{sc} (Figure 8c,d), indicating no significant changes in passivation quality or optical transmission.

In contrast, the efficiency of ECT-2 modules decreased by around 2% during the first 100 cycles, after which it stabilized. This initial loss was primarily attributed to a reduction in FF (Figure 8b). The efficiency trend closely paralleled the change in contact resistance observed during the TC test, suggesting that contact degradation was the primary cause of the FF reduction in ECT-2 modules.

As with the DH test, we compared the EL images of the modules before and after the 200-cycle TC test, as shown in Figure 9. As all modules deteriorate slightly during the TC test, the changes in the EL images are not obvious. Nevertheless, we identified some inhomogeneity in the EL images near the ribbon of the modules with ECT-2 and low-melting solder, indicated by in green and purple circles. This suggests a decline in local contact. This also corresponds to the decline in the R_c measurement results. To highlight the changes more visibly, we illustrate and compare the EL signal intensity along the lines shown in Figures S4 and S5.

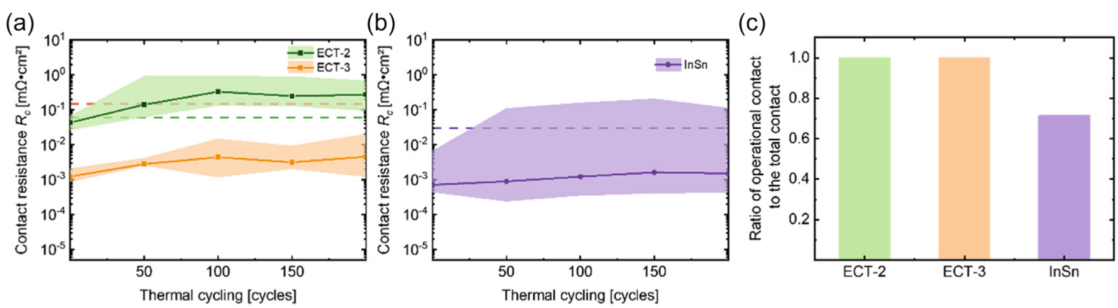

FIGURE 7 | Evolution of contact resistance during thermal cycling for ECT-2 and ECT-3 (a) and for InSn solder used as a reference (b). The ratio of operational contacts to total contacts after testing is shown in (c).

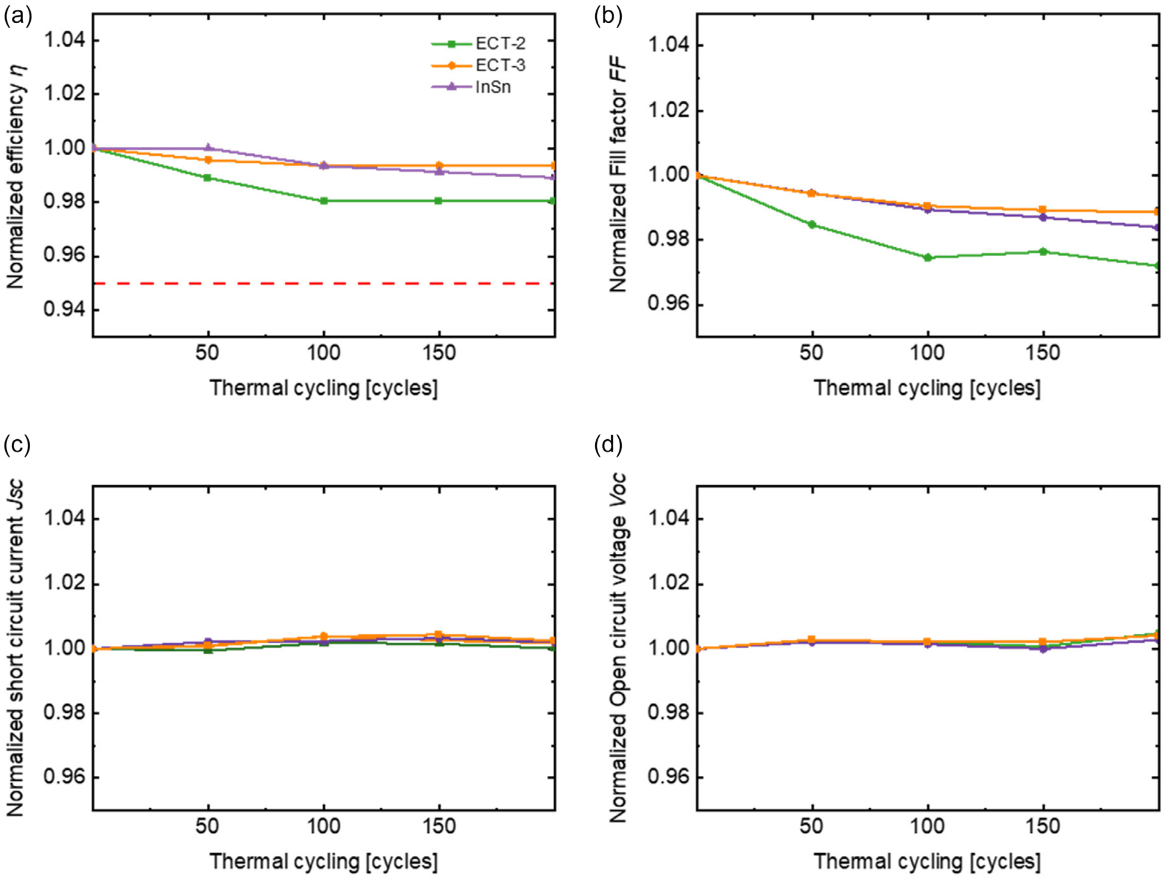

FIGURE 8 | Relative changes in (a) efficiency, (b) fill factor, (c) short-circuit current density, and (d) open-circuit voltage of SHJ modules with different interconnection methods during TC testing as indicated in the legend.

3.6 | The Comparison of Adhesion of Different ECTs

According to DIN EN 50461, solar cell interconnects must withstand a minimum pull force of 1 N/mm [10]. This peel-force requirement is widely recognized as a benchmark for assessing the interconnection quality in PV modules. Following the electrical performance evaluation, Figure 10 presents a boxplot summarizing the peel force measured along the 5 cm ECTs and compares the peel strength of three ECTs bonded to the solar cell busbar.

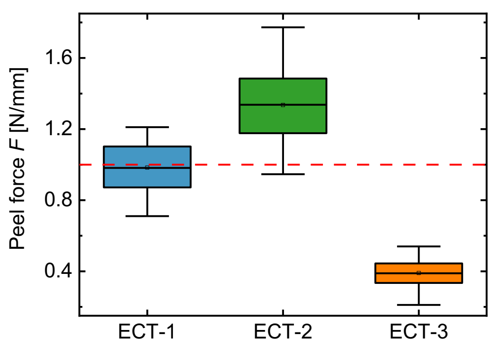

FIGURE 10 | Comparison of peel force between tabbing ribbons and the busbar for different ECTs.

Among the tested tapes, ECT-2 exhibited the strongest adhesion, consistently exceeding the 1 N/mm requirement along the full

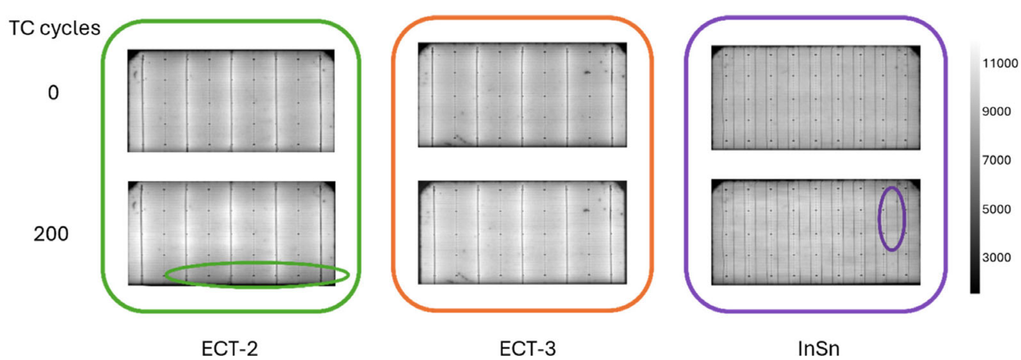

FIGURE 9 | EL images of solar modules initially and after 200 cycles of thermal cycling testing.

ribbon length, with a peak value of 1.8 N/mm. ECT-1 performed moderately, fluctuating near the standard and reaching a maximum of 1.2 N/mm. In contrast, ECT-3 exhibited the weakest adhesion, consistent with earlier findings, despite previously delivering the lowest and most stable contact resistivity.

In PV applications, robust adhesion is essential for automated manufacturing processes [18], while the electrical stability of interconnections is critical for ensuring consistent power generation throughout a module's lifetime. Based on our studies, ECT-2 is better suited for PV applications, as it meets all requirements for solar cell interconnection in solar modules, offering a balance of strong adhesion and reliable electrical performance. Nevertheless, ECT-3 shows promise as a cost-effective interconnection material. By optimizing the adhesive formulation or adjusting the balance between particle size and adhesive thickness, the adhesion performance of ECT-3 could be enhanced to meet the 1 N/mm criterion, potentially making it a viable alternative for PV applications.

3.7 | Comparison of the Microstructure of ECTs

To better understand the differences in electrical and mechanical performance among the investigated ECTs, both optical microscopy and cross-sectional SEM analyses were performed. The optical microscopy images shown in Figure S1 were used to quantify the distribution of conductive particles within the adhesive layer. Within an analyzed area of 0.7 × 0.5 mm, ECT-2 contained 56 conductive particles with diameters exceeding the adhesive thickness, corresponding to an estimated particle coverage ratio of approximately 11.5%. In contrast, ECT-3 contained only 17 such particles within the same area, corresponding to a considerably lower coverage ratio of approximately 2.0%.

Despite this lower particle coverage ratio, ECT-3 consistently exhibited lower contact resistance than ECT-2. This finding suggests that electrical performance is not primarily governed by the number of conductive particles per unit area. Instead, the ratio between particle size and adhesive thickness appears to be the dominant factor. In ECT-3, the adhesive layer thickness is only 10 μm, whereas the Ni particles have diameters ranging from approximately 20–50 μm. Consequently, many particles are significantly larger than the adhesive thickness and can penetrate through the adhesive layer, forming direct electrical bridges between the ribbon and the busbar. In contrast, ECT-2 contains a 50 μm adhesive layer with Ag particles of approximately 30–60 μm in diameter. As a result, a larger fraction of adhesive material remains between the conductive particles and the contacting surfaces, increasing the electrical transport distance. While this structure promotes stronger mechanical bonding through a larger effective adhesive contact area, it is less favorable for minimizing contact resistance.

Figure 11 presents cross-sectional SEM images of the contact regions formed using the three ECT types. For the isotropic ECT-1 shown in Figure 11a, several voids can already be observed both at the interfaces and within the conductive layer before the DH test. Since current must pass through the polymer matrix to reach the embedded conductive mesh and subsequently travel through the lower adhesive layer, these voids locally interrupt conductive pathways. As a result, the effective conductive area is reduced, leading to increased contact resistance. In contrast, ECT-2 and ECT-3 in Figure 11c,d are anisotropic conductive tapes, where electrical conductivity is established through metallic particles bridging the two contacting surfaces. The SEM images reveal a larger separation between ribbon and busbar for ECT-2 than for ECT-3, consistent with their respective adhesive thicknesses. In ECT-2, the Ag particles are largely embedded within the adhesive layer, allowing the adhesive to encapsulate the particles and create a robust mechanical bond. Consequently, no significant voids are observed, and ECT-2 exhibits the highest adhesion strength among the investigated tapes. For ECT-3, the Ni particles frequently penetrate through the adhesive layer and establish more direct electrical contacts between the ribbon and busbar. This morphology explains the lower contact resistance observed experimentally. However, the reduced adhesive volume at the interface also decreases the effective bonding area, resulting in lower adhesion strength compared to ECT-2.

To investigate the degradation mechanism of the isotropic ECT-1, additional cross-sectional SEM analyses were performed after 1000 h of damp-heat exposure, as shown in Figure 11b. Compared with the initial microstructure, the aged samples exhibit a noticeably larger number of voids at the interface between the conductive tape and the ribbon. These voids are particularly pronounced at the bottom of the ribbon texture, where intimate contact between the conductive adhesive and the metallic surface is most critical. The increased interfacial void density indicates progressive interfacial debonding during damp-heat exposure, resulting in a reduction of the effective electrical contact area. Consequently, conductive pathways are disrupted and the current transport resistance across the interface increases. This observation is consistent with the measured increase in contact resistance by more than two orders of magnitude during damp-heat testing and the corresponding performance degradation observed at module level. Therefore, interfacial debonding and void formation are considered the primary degradation mechanisms responsible for the electrical deterioration of ECT-1 under damp-heat conditions.

Overall, these observations indicate a trade-off between electrical and mechanical performance. ECT-3 favors electrical conductivity by maximizing direct particle-mediated contact, whereas ECT-2 provides superior mechanical robustness through a larger adhesive bonding area. This interpretation is consistent with the measured contact-resistance and peel-force results presented in Sections 3.3 and 3.6. Furthermore, the post-aging analysis demonstrates that the long-term stability of conductive tapes is strongly influenced by the ability of the adhesive interface to maintain intimate contact under environmental stress.

3.8 | Comparison With Other Solder-Free Interconnection Technologies

To place the performance of ECTs into the broader context of PV module interconnection, their electrical performance, reliability, cost, and processability were compared with other state-of-the-art solder-free interconnection technologies, including ECAs and TECC wires.

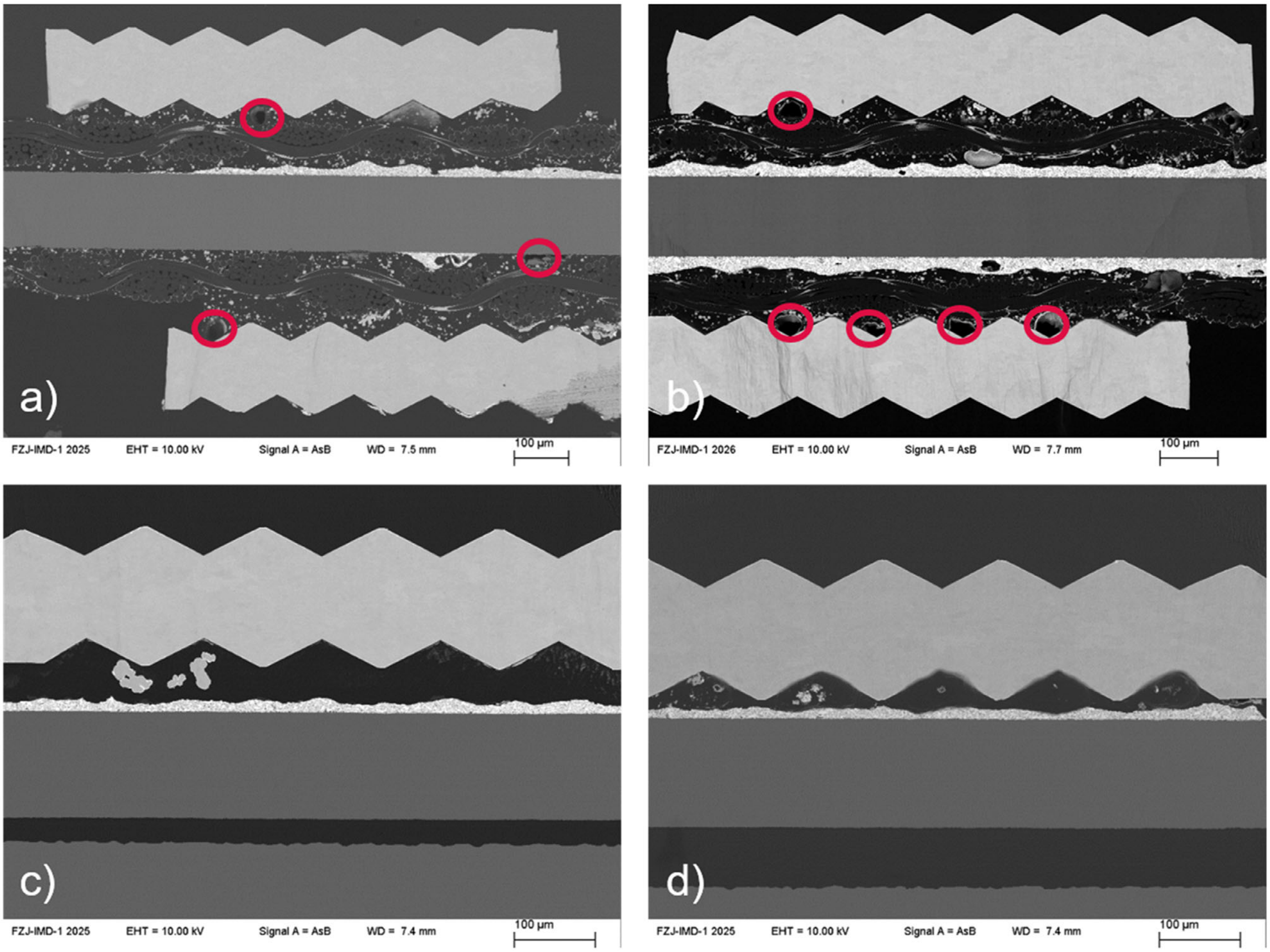

FIGURE 11 | Cross-sectional SEM images of the contact regions formed using ECT-1 before damp heat test in (a), ECT-1 after damp heat test in (b), ECT-2 in (c), and ECT-3 in (d).

From an electrical perspective, ECTs demonstrated sufficiently low contact resistance for PV applications. In this work, ECT-3 exhibited contact resistance values in the range of 10^{-3}–10^{-2} mΩ·cm^2 before aging. For comparison, commercially available ECAs evaluated using the same measurement method exhibited contact resistance values in the range of 10^{-5} mΩ·cm^2. Although ECAs can achieve lower contact resistance, both technologies provide values substantially below the failure thresholds identified by the PVMOS simulations in Figure 2. Consequently, from a practical module-performance perspective, the electrical performance of both approaches is sufficient.

In terms of reliability, the anisotropic ECTs investigated in this study exhibited less than 5% relative efficiency degradation after 2000 h of damp-heat testing and 200 thermal cycles. This performance is comparable to previously reported TECC-wire interconnection concepts, which showed approximately 3% relative degradation after 2000 h of damp-heat exposure [19]. These results indicate that ECTs can achieve a reliability level comparable to other advanced solder-free interconnection technologies.

A preliminary material cost comparison was performed for a 22.5%-efficient M2 nine-busbar module configuration. Assuming ECT-2 is applied only at the buspads, the corresponding interconnection material cost is approximately 0.85 €cent/W. For comparison, an ECA-based interconnection using a 40 µm adhesive layer results in an estimated material cost of approximately 2.27 €cent/W. Under these assumptions, the ECA solution is approximately 2.7 times more expensive than the ECT solution in terms of interconnection material cost alone.

From a manufacturing perspective, each technology offers distinct advantages. TECC wires can be integrated into existing stringing equipment with relatively minor modifications, while industrial high-throughput dispensing and stringing systems for ECAs are already commercially available, although they remain more expensive than conventional soldering equipment. In contrast, ECT technology is currently less mature for PV manufacturing. To minimize optical shading, ECTs must be applied as narrow and accurately positioned strips, either directly onto the solar cell or integrated onto the interconnection ribbon. At present, dedicated high-throughput equipment for such processes is not widely available, representing one of the main challenges for large-scale industrial implementation.

Nevertheless, ECTs offer several unique advantages compared with both ECAs and TECC wires. Unlike ECA-based approaches, no additional thermal curing step is required after application. Furthermore, unlike TECC-wire concepts, no pre-coating of

TABLE 1 | IV characteristics of the perovskite-SHJ tandem solar cell and module.

	η, %	FF, %	J_{sc}, mA/cm^2	V_{oc}, V
Cell	29.9	76.7	20.7	1.88
Module	28.6	79.2	19.2	1.88

the whole interconnection wires with conductive adhesive is necessary. Instead, both the electrical and mechanical contacts can be established directly during the standard module lamination process. This simplified process flow is particularly attractive for thermally sensitive PV technologies, such as perovskite–silicon tandem solar cells, where minimizing thermal exposure is essential. Consequently, ECTs represent a promising low-temperature interconnection technology, provided that suitable high-throughput application processes can be developed for industrial production.

3.9 | Perovskite-SHJ Tandem Solar Cell Using ECT as Electrical Contact

Having successfully tested the properties of ECTs on SHJ solar cells, we extended their application to perovskite-SHJ tandem solar cells. To this end, we contacted and encapsulated 1 cm × 1 cm perovskite/silicon tandem solar cells. ECT-2 was applied to the front Ag electrode frame, which serves as a busbar to collect current from the thin fingers (Section S6). As ECT-2 does not require additional heat treatment, the single-cell module was laminated at the minimum temperature needed for the physical cross-linking of the thermoplastic polyolefin (TPO) encapsulation material (90 °C for 10 min). The IV characteristics and curves are summarized in Table 1 and Section S7. The module efficiency decreased by approximately 1.3% compared to the bare cell, primarily due to a reduction in short-circuit current density from 20.7 to 19.2 mA/cm^2. This reduction stems from optical losses: although the cells were coated with an MgF_2 AR layer to minimize reflection at the ITO/air interface, this AR effect is diminished upon encapsulation, and the front glass of the module lacked an AR coating. However, the lower current density led to an improved FF, which increased from 76.7% to 79.2%, as power losses associated with series resistance decrease with reduced current. Overall, these findings highlight ECT-2 as a promising interconnection strategy for perovskite-SHJ tandem solar cells, eliminating the need for the high-temperature curing step required by conventional ECAs.

4 | Conclusion

This study investigated the feasibility of using ECTs as a solder-free interconnection technology for thermally sensitive PV devices, focusing on SHJ solar cells. The influence of lamination temperature and pressure on adhesion and contact resistance was systematically evaluated, and long-term stability was assessed through DH and TC tests in accordance with IEC 61215 standards [11]. Our results demonstrate that ECTs can provide sufficiently low contact resistance—comparable to that of low-melting-point solders—while eliminating the need for heat-intensive processing steps. Among the tested tapes, with differences in thickness and conductive material, anisotropic ECT-2 and ECT-3 exhibited stable electrical performance throughout extended DH and TC testing, remaining below the failure thresholds predicted by simulation. In particular, ECT-3, which is the thinnest, achieved the lowest and most stable contact resistance, while ECT-2 offered the strongest adhesion, most likely due to the thicker adhesive layer, exceeding the 1 N/mm criterion of DIN EN 50461 [10]. In contrast, isotropic ECT-1 showed rapid degradation under DH stress, indicating that anisotropic designs are probably more suitable for PV interconnections.

Module-level testing further validated the potential of ECTs for industrial application. SHJ modules interconnected with ECT-2 and ECT-3 maintained efficiency losses of less than 5% relative even after 2000 h of DH exposure and 200 thermal cycles (as summarized in Section S8), matching or outperforming soldered references. EL imaging confirmed that contact degradation in ECT-based modules was significantly less pronounced than in soldered counterparts.

Overall, these findings suggest ECTs as an advantageous approach toward reliable, low-temperature, and scalable interconnection technology for next-generation PV modules, particularly SHJ and perovskite-Si tandem devices, where thermal sensitivity restricts the use of conventional soldering. Future optimization of the adhesive composition and the particle geometry could further improve the balance between electrical stability and mechanical adhesion, accelerating the adoption of anisotropic conductive tapes in commercial SHJ and perovskite-Si solar module manufacturing.

Acknowledgments

We appreciate the financial support of Bundesministerium für Wirtschaft und Klimaschutz through the Supersolid Project [03EE1181B].

Open Access funding enabled and organized by Projekt DEAL.

Funding

This study was supported by Bundesministerium für Wirtschaft und Energie (03EE1181B).

Conflicts of Interest

The authors declare no conflicts of interest.

Data Availability Statement

The data that support the findings of this study are available from the corresponding author upon reasonable request.

References

1. S. De Wolf, A. Descoeudres, Z. C. Holman, and C. Ballif, "High-Efficiency Silicon Heterojunction Solar Cells: A Review," *Green* 2 (2012): 7–24, https://doi.org/10.1515/green-2011-0018.

2. R. Witteck, D. Nguyen Minh, G. Paul, et al., "Reducing Thermal Degradation of Perovskite Solar Cells During Vacuum Lamination by Internal Diffusion Barriers," *ACS Applied Energy Materials* 7 (2024): 10750–10757, https://doi.org/10.1021/acsaem.4c02567.

3. A. Faes, L. Curvat, H. Li, et al., “Direct Contact to TCO with SmartWire Connection Technology,” in 2018 IEEE 7th World Conference on Photovoltaic Energy Conversion, WCPEC 2018 - A Joint Conference of 45th IEEE PVSC, 28th PVSEC and 34th EU PVSEC, 2018, 1998–2001, https://doi.org/10.1109/PVSC.2018.8547406.

4. D. Güldali, A. De Rose, M. Mittag, B. Grübel, H. Neuhaus, and U. Tetzlaff, “Interconnection of Low-Temperature Metallization on Silicon Solar Cells - the Role of Silver in Tin-Bismuth-Based Solder Alloys,” *Solar Energy Materials and Solar Cells* 285 (2025): 113488, https://doi.org/10.1016/J.SOLMAT.2025.113488.

5. Y. Liu, I. M. Peters, K. Ding, et al., “Silver Reduction Through Direct Wire Bonding for Silicon Heterojunction Solar Cells,” *Solar Energy Materials and Solar Cells* 282 (2025): 113412, https://doi.org/10.1016/J.SOLMAT.2025.113412.

6. A. De Rose, T. Geipel, D. Eberlein, et al., “Interconnection of silicon heterojunction solar cells by infrared soldering-solder joint analysis and temperature study,” in 2018 IEEE 7th World Conference on Photovoltaic Energy Conversion (WCPEC) (A Joint Conference of 45th IEEE PVSC, 28th PVSEC & 34th EU PVSEC) (accessed 2025 September 10), https://publica-rest.fraunhofer.de/server/api/core/bitstreams/fa92d16c-4773-4071-843b-8290b9060ab6/content.

7. RoHS Directive - European Commission, n.d., (accessed September 10, 2025), https://environment.ec.europa.eu/topics/waste-and-recycling/rohs-directive_en.

8. Y. Zemen, L. Podlowski, S. Wendlandt, and J. Stegmann, “Thermoplastically and Electrically Conductive Coated Wire for the Interconnection of Temperature- Sensitive Solar Cells,” in Conference Record of the IEEE Photovoltaic Specialists Conference (2021), 0480–485, https://doi.org/10.1109/PVSC43889.2021.9518596.

9. Y. Li, D. Lu, and C. P. Wong, “Chapter 5—Anisotropically Conductive Adhesives/Films (ACA/ACF),” in *Electrical Conductive Adhesives with Nanotechnologies* (Springer, 2010).

10. DIN EN 50461 - 2007-03 - DIN Media, 2025, https://www.dinmedia.de/de/norm/din-en-50461/96457922.

11. DIN EN IEC 61215-1 - 2022-02 - DIN Media, 2025, https://www.dinmedia.de/de/norm/din-en-iec-61215-1/347094343.

12. M. Devoto, K. Wienands, D. Rudolph, et al., “Validation of Methodology to Determine the Contact Resistivity of ECA-Based Bonds Grounded on End–Contact Resistance Measurements Using Redundant and Modified TLM Test Structures,” *Solar Energy Materials and Solar Cells* 262 (2023): 112518, https://www.sciencedirect.com/science/article/pii/S0927024823003392.

13. A. De Rose, A. Kraft, S. Gledhill, et al., “Solder Interconnection of Aluminum Foil Rear Side Metallization for Passivated Emitter and Rear Solar Cells,” in 7th Workshop on Metallization and Interconnection for Crystalline Silicon Solar Cells (2017), https://papers.ssrn.com/sol3/papers.cfm?abstract_id=3152428.

14. B. E. Pieters, “A Free and Open Source Finite-Difference Simulation Tool for Solar Modules,” in 2014 IEEE 40th Photovoltaic Specialist Conference (PVSC, 2014), https://doi.org/10.1109/PVSC.2014.6925173.

15. A. De Rose, D. Erath, V. Nikitina, et al., “Low-Temperature Metallization & Interconnection for Silicon Heterojunction and Perovskite Silicon Tandem Solar Cells,” *Solar Energy Materials and Solar Cells* 261 (2023): 112515, https://doi.org/10.1016/j.solmat.2023.112515.

16. P. Hacke, D. C. Miller, D. Pierpont, and T. Wu, “Performance and Durability of Electrically Conductive Tape for Shingled Si Heterojunction Technology Cells,” *Progress in Photovoltaics: Research and Applications* 33 (2025): 16–26, https://doi.org/10.1002/PIP.3749.

17. C. Sen, H. Wang, X. Wu, et al., “Four Failure Modes in Silicon Heterojunction Glass-Backsheet Modules,” *Solar Energy Materials and Solar Cells* 257 (2023): 112358, https://doi.org/10.1016/J.SOLMAT.2023.112358.

18. T. Geipel, V. Nikitina, L. P. Bauermann, et al., “Industrialization of Ribbon Interconnection for Silicon Heterojunction Solar Cells With Electrically Conductive Adhesives,” in EU PVSEC 2019 (2019), https://doi.org/10.4229/EUPVSEC20192019-4CO.3.3.

19. Y. Zemen, S. Wendlandt, B. Litzenburger, and L. Podlowski, “WCPEC-8, undefined Session, undefined 2022, Interconnection Technology for the Next Generation of (Temperature-Sensitive) Solar Cells Such as Heterojunction and C-Si/Perovskite Tandem,” in 8th World Conference on Photovoltaic Energy Conversion (accessed June 11, 2026), https://www.researchgate.net/profile/Stefan-Wendlandt-2/publication/364324141_Interconnection_Technology_for_the_Next_Generation_of_Temperature-Sensitive_Solar_Cells_such_as_Heterojunction_and_C-SiPerovskite_Tandem/links/639dcbc1e42faa7e75cebbc0/Interconnection-Technology-for-the-Next-Generation-of-Temperature-Sensitive-Solar-Cells-such-as-Heterojunction-and-C-Si-Perovskite-Tandem.pdf.

Supporting Information

Additional supporting information can be found online in the Supporting Information section.